







Article

Simulation, Structural, Thermal and Mechanical Properties of the FeTiTaVW High Entropy Alloy

Ricardo Martins ¹, António Pereira Gonçalves ², José Brito Correia ³, Andrei Galatanu ⁴, Eduardo Alves ¹, Elena Tejado ⁵, José Ygnacio Pastor ⁵ and Marta Dias ^{1,*}

- ¹ Instituto de Plasmas e Fusão Nuclear, Instituto Superior Técnico, Universidade de Lisboa, Av. Rovisco Pais, 1049-001 Lisboa, Portugal; ricardo.martins@ctn.tecnico.ulisboa.pt (R.M.); ealves@ctn.tecnico.ulisboa.pt (E.A.)
- ² C²TN, Instituto Superior Técnico, Universidade de Lisboa, Campus Tecnológico e Nuclear, Estrada Nacional 10, 2695-066 Bobadela LRS, Portugal; apg@ctn.tecnico.ulisboa.pt
- ³ LNEG, Laboratório Nacional de Energia e Geologia, Estrada do Paço do Lumiar, 1649-038 Lisboa, Portugal; brito.correia@lneg.pt
- ⁴ National Institute of Materials Physics, 077125 Magurele, Romania; gala@infim.ro
- ⁵ Departamento de Ciencia de Materiales-CIME, ETSI Caminos, Canales y Puertos, Universidad Politecnica de Madrid, 28040 Madrid, Spain; elena.tejado@upm.es (E.T.); jy.pastor@upm.es (J.Y.P.)
- * Correspondence: marta.dias@ctn.tecnico.ulisboa.pt or marta.dias@ctn.ist.utl.pt

Abstract: Developing new materials to be applied in extreme environments is an opportunity and a challenge for the future. High entropy alloys are new materials that seem promising approaches to work in nuclear fusion reactors. In this work, FeTaTiVW high entropy alloys were developed and characterized with Molecular Dynamic and Hybrid Molecular Dynamic Monte Carlo simulations. The simulation results show that phase separation originates a lower potential energy per atom and a high level of segregation compared to those of a uniform solid solution. Moreover, the experimental diffractogram of the milled powder shows the formation of a body-centred cubic-type structure and the presence of TiO₂. In addition, the microstructure of the consolidated material evidenced three phases: W-rich, Ti-rich, and a phase with all the elements. This phase separation observed in the microstructure agrees with the Hybrid Molecular Dynamic Monte Carlo simulation. Moreover, the consolidated material's thermal conductivity and specific heat are almost constant from 25 °C to 1000 °C, and linear expansion increases with increasing temperature. On the other hand, specific heat and thermal expansion values are in between CuCrZr and W values (materials chosen for the reactor walls). The FeTaTiVW high entropy alloy evidences a ductile behaviour at 1000 °C. Therefore, the promising thermal properties of this system can be attributed to the multiple phases and systems with different compositions of the same elements, which is exciting for future developments.

Keywords: high entropy alloys; molecular dynamics simulation; hybrid molecular dynamic Monte Carlo; thermal properties; mechanical properties



Citation: Martins, R.; Gonçalves, A.P.; Correia, J.B.; Galatanu, A.; Alves, E.; Tejado, E.; Pastor, J.Y.; Dias, M. Simulation, Structural, Thermal and Mechanical Properties of the FeTiTaVW High Entropy Alloy. *Metals* **2024**, *14*, 436. <https://doi.org/10.3390/met14040436>

Academic Editors: Chao Yang and Jiro Kitagawa

Received: 4 March 2024

Revised: 26 March 2024

Accepted: 30 March 2024

Published: 8 April 2024



Copyright: © 2024 by the authors. Licensee MDPI, Basel, Switzerland. This article is an open access article distributed under the terms and conditions of the Creative Commons Attribution (CC BY) license (<https://creativecommons.org/licenses/by/4.0/>).

1. Introduction

The necessity of materials to be applied to the nuclear reactor is essential nowadays to produce energy. Therefore, materials that can withstand intense heat flows must collect the generated heat without compromising structural integrity. Until now, W has been chosen as a plasma plasma-facing component (in the divertor) due to its high melting point, low sputter yield, and low tritium retention [1]. However, a harmful issue associated with W is its high ductile-to-brittle transition temperature (DBTT). In addition, a CuCrZr alloy has been selected as a heat sink for the power absorbed by the plasma-facing components [2]. However, this material suffers embrittlement under irradiation [3], and its allowed service temperature is relatively low [4]. Therefore, an intermediate layer is required to guarantee adequate thermal transport between both materials while keeping their temperatures at the proper working intervals.

The development of technology has led to the gradual but obvious conclusion that conventional alloys have nearly reached their performance limits and can no longer meet the demands of present-day applications. In response to this challenge, the development of new materials, such as high entropy alloys (HEAs), that have shown promising characteristics has risen. Unlike conventional alloys, they contain five or more elements and, in most cases, were found to possess single-phase microstructures face-centred-cubic (fcc) [5], body-centred-cubic (bcc) [6], hexagonal-closed-packed (hcp) type-structure [7], emerging as a new research frontier for explorations of novel materials with outstanding properties. The enhanced stability of solid solutions in HEAs can be attributed to the high entropy of mixing, which lowers their relative Gibbs Free Energy and promotes their stability [8,9]. Compared to their conventional alloy counterparts, high entropy alloys have demonstrated superior physical and mechanical properties [10]. High-entropy alloys offer remarkable features, including high strength, even at elevated temperatures such as in NbMoTaW and VNbMoTaW [11] and exceptional thermal stability as found in nickel-based alloys ($\text{Ni}_{80}\text{Mo}_{6.6}\text{Ti}_6\text{Nb}_6\text{Ta}_{1.4}$), ($\text{Ni}_{29}\text{Fe}_{23}\text{Co}_{23}\text{Cr}_{23}\text{Zr}_2$ and $\text{Ni}_{25}\text{Fe}_{23}\text{Co}_{23}\text{Cr}_{23}\text{Mo}_2\text{Nb}_2\text{Zr}_2$) [12]. Moreover, owing to their impressive blend of mechanical properties, HEAs are considered promising candidates for a wide range of advanced engineering applications, including nuclear reactors, as is the case of (TaTiVZr)X (X = Hf or W) [13] and $\text{Ti}_2\text{ZrHfV}_{0.5}\text{Mo}_{0.2}$ [14].

Molecular Dynamics (MD) is a computational simulation technique used to calculate the properties of a many-body system. In MD, each atom is assumed to be a point mass, and the motion of atoms is determined by Newton's equation [15]. The Monte Carlo simulation method randomly swaps atom positions to achieve a more stable overall configuration. Hybrid MD-MC simulations, combining Molecular Dynamics and Monte Carlo, have been used for simulating HEAs [16]. The LAMMPS software (64-bit 22Dec2022) can perform MD and MC simulations and simulate X-ray diffraction patterns based on atomistic simulation results [17,18]. The interaction between atoms can be described using an embedded atom method (EAM) potential, which assumes that the energy of a solid is a function of the electron density. The EAM potential correlates well with more precise bonding methods and can be used for metals [15,19,20].

This work presents the simulation by MD and MC together with the development and characterization of a FeTaTiVW high entropy alloy. The structural characterization was performed using scanning electron microscopy and X-ray diffraction on the milled powder and on the consolidated samples. Moreover, the thermal and mechanical properties of consolidated samples were also evaluated and discussed.

2. Experimental Details

An equimolar Fe-Ta-Ti-V-W alloy was simulated using periodic boundary conditions. The software LAMMPS (64-bit 22Dec2022) of Sandia Labs was used for (a) Molecular Dynamics and (b) hybrid Molecular Dynamic/Monte Carlo simulations. The bcc structure was assumed for the simulations (13^3 cells), and the number of atoms was 4394. The typical simulation sequence involved several steps of energy minimization of the initial configuration, heating to the simulation temperature, and energy minimization for 6×10^6 time steps. The Hybrid Molecular Dynamic/Monte Carlo simulation, hereafter referred to as MC, consisted of the introduction of a Monte Carlo swap attempt every 10 Molecular Dynamic simulation steps (MC 10:1). The temperature used in the Metropolis criterion dictating swap probabilities was the same as that used in the MD simulation. The pressure was maintained at 1 atmosphere. The EAM potential for Fe-Ta-Ti-W was retrieved from NIST [21], referring to the original work of Zhou et al. [22]. The same procedure, using the same data set for the simulation of multicomponent alloys, has already been reported in the literature [21]. As the EAM set potential used [22] does not include vanadium, a hybrid potential (force field) was developed [23] in which the interactions involving vanadium were described by the Mie potential (a central potential related to the Lennard–Jones potential) with the parameters published in [23].

Powders of Fe, Ti, Ta, V (AlfaAesar, 99.9% nominal purity with average particle size 10 μm) and W (AlfaAesar, 99.9% nominal purity with an average particle size 10 μm and 35–55 nm) were mixed in the adequate proportion: FeTaTiVW in a glove box and mechanically alloyed in a high-energy planetary ball mill, PM 400 MA, with WC balls and vials. The balls-to-powder mass ratio was 10:1, and the milling was performed at 350 rpm (rotations per minute) for two hours. No process control agent (PCA) was used. The sample and the respective atomic percentages are shown in Table 1.

Table 1. Atomic percentage of each element in the sample.

Designation	Fe (at.%)	Ta (at.%)	Ti (at.%)	V (at.%)	W (at.%)
FeTaTiVW	20	20	20	20	20

The as-milled powders were then consolidated by Spark-Plasma Sintering (SPS) on an FCT Systeme Gmbh sintering machine in a condition shown in Table 2.

Table 2. SPS conditions for each composition.

Designation	Temperature ($^{\circ}\text{C}$)	Force (kN)	Holding Time (min)
FeTaTiVW	1100	9	5

After sintering, the apparent density was measured using Archimedes' method [24] at room temperature in water. The theoretical density of FeTaTiVW high entropy alloy was calculated based on [25] at 11.18 g/cm^3 .

Metallographic preparation of the samples was performed by grinding with SiC paper and polishing with diamond suspensions (6 μm , 3 μm and 1 μm). Finally, the fine polish was achieved with colloidal silica suspension (0.2 μm). The microstructures were observed by secondary electrons (SE) and backscattered electrons (BSE) using a JEOL JSM-7001F field emission gun SEM equipped with an Oxford EDS spectrometer.

Powder X-ray diffraction (PXRD) was used to investigate the evolution of the powders' mixtures using a Philips X'Pert diffractometer in a Bragg-Brentano geometry with Cu K_α radiation over a 2θ range from 10° to 100° with a 2θ step size of 0.03° .

The high-temperature thermal properties have been investigated using a laser flash analyser (LFA 457, Netzsch, Selb, Germany) from room temperature up to 1000°C , and the expansion coefficients have been determined in the same temperature range using a Netzsch 402C dilatometer. The LFA equipment allows for direct measurement of the thermal diffusivity, while the specific heat of materials can be determined by a differential method using a reference sample (NIST Mo SRM-781).

Quasi-static three-point bending (TPB) tests were then performed on smooth bars of $0.8 \times 1.2 \text{ mm}^2$ section cut by electro-discharge machining. A loading span of 10 mm and a constant cross-head travel speed of 100 $\mu\text{m}/\text{min}$ were selected for quasistatic testing. To characterise the mechanical behaviour of these novel materials in their expected operating temperature range, TPB tests were performed at 25°C , 600°C and 1000°C under a high vacuum atmosphere (10^{-6} mbar). The flexural strength was later computed using Euler-Bernoulli equations for slender beams up to failure, and their fracture surfaces were evaluated.

Vickers microhardness was obtained by applying a load of 200 gf for 15 s on an AKASHI MVK-EIII tester. Additionally, nanoindentation to a depth of 1500 nm was performed on the same samples using a standard Berkovich tip, calibrated using fused silica. The hardness measurements were performed on random regions. The average values of hardness and elastic modulus were taken from the unloading curve following the Oliver and Pharr method [26]. The Young Modulus of the HEA sample was obtained from the reduced modulus of the system (E_r) (calculated from the unloading contact stiffness), the

young modulus of the diamond indenter (E_i), and the poisson ratio of both samples (ν_s), and indenter (ν_i), as in [27] using the following expression:

$$\frac{1}{E_r} = \frac{1 - \nu_s^2}{E_s} + \frac{1 - \nu_i^2}{E_i} \quad (1)$$

For the calculations, a poisson ratio of 0.3 was used for the HEA sample. Thermodynamics calculations were first performed to determine the possible structures formed in the alloys and to help with the interpretation and discussion of the results. Based on empirical models [28,29] using the enthalpies and entropies of mixing, ΔH_{mix} and ΔS_{mix} , the fractional atomic size differences δ and the valence electron concentrations, VEC, it is possible to predict the formation of solid solutions in the ranges $-15 \text{ kJ/mol} \leq \Delta H_{mix} \leq 5 \text{ kJ/mol}$, $11 \text{ J/(K}\cdot\text{mol)} \leq \Delta S_{mix} \leq 19.5 \text{ J/(K}\cdot\text{mol)}$, and $1 \leq \delta \leq 6$: the stable most phases are predicted to be fcc at $\text{VEC} \geq 8$ and bcc at $\text{VEC} < 6.87$. Between these values, mixed fcc and bcc type-structures are expected to coexist. In this context, the calculations of the relevant properties of Fe-Ta-Ti-V-W multicomponent alloy are presented in Table 3. Based on the calculated values, the existence of a bcc solid solution is expected for the FeTaTiVW and compositions.

Table 3. Thermodynamic calculations for FeTaTiVW multicomponent alloy.

Designation	ΔH_{mix}	ΔS_{mix}	δ	VEC
FeTaTiVW	-8.8 kJ/mol	$13.4 \text{ J/(K}\cdot\text{mol)}$	5.8	5.6

3. Results and Discussion

3.1. Simulation

Molecular Dynamic (MD) simulation was performed similarly to previous research [30,31]. The variation of average potential energy per atom with simulation temperature is shown in Figure 1 for both MD and MC simulations. Hybrid molecular dynamic Monte Carlo (MC) simulation resulted in general phase separation, essentially titanium segregation, corresponding to an average potential energy per atom smaller than that of MD simulations. A difference in potential energy of about 0.15 eV at low temperatures clearly shows that the MC simulation yields the lower potential energy.

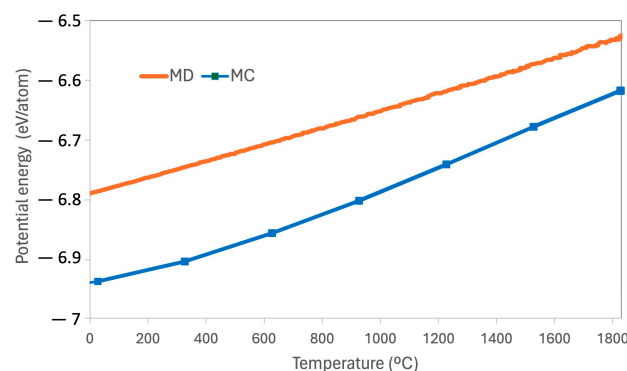


Figure 1. Potential energy versus temperature for the MD and MC simulations.

Figure 2a shows the MD structure obtained for the simulation at 25 °C. Random distribution of the five elements, similar to that of the starting structure, can be observed. In contrast, Figure 2b shows a segregated structure resulting from MC simulation. In Figure 2c,d, the Pair Distribution Function, $g(r)$, of the different pairs of elements is shown. Regarding a single element, the most evident feature from the analysis of MC simulation (Figure 2d) for the first near neighbours (NN) is titanium segregation (very high probability of a Ti–Ti bond). This effect can be explained since, in MC simulation, there are no diffusion barriers and the formation of a separate Ti phase yielding a lower average potential energy

for the ensemble is permitted. However, in MD simulation, the movement is restricted to the physical diffusion of the elements. In both types of simulation, the crystal structure obtained was entirely bcc type-structure. The lattice parameters extracted from the simulation cells were 0.3091 nm for MC and 0.3099 nm for MD at 25 °C. The densities extracted from the simulations were, respectively, 12.08 g/cm³ and 11.98 g/cm³ for MC and MD at 25 °C.

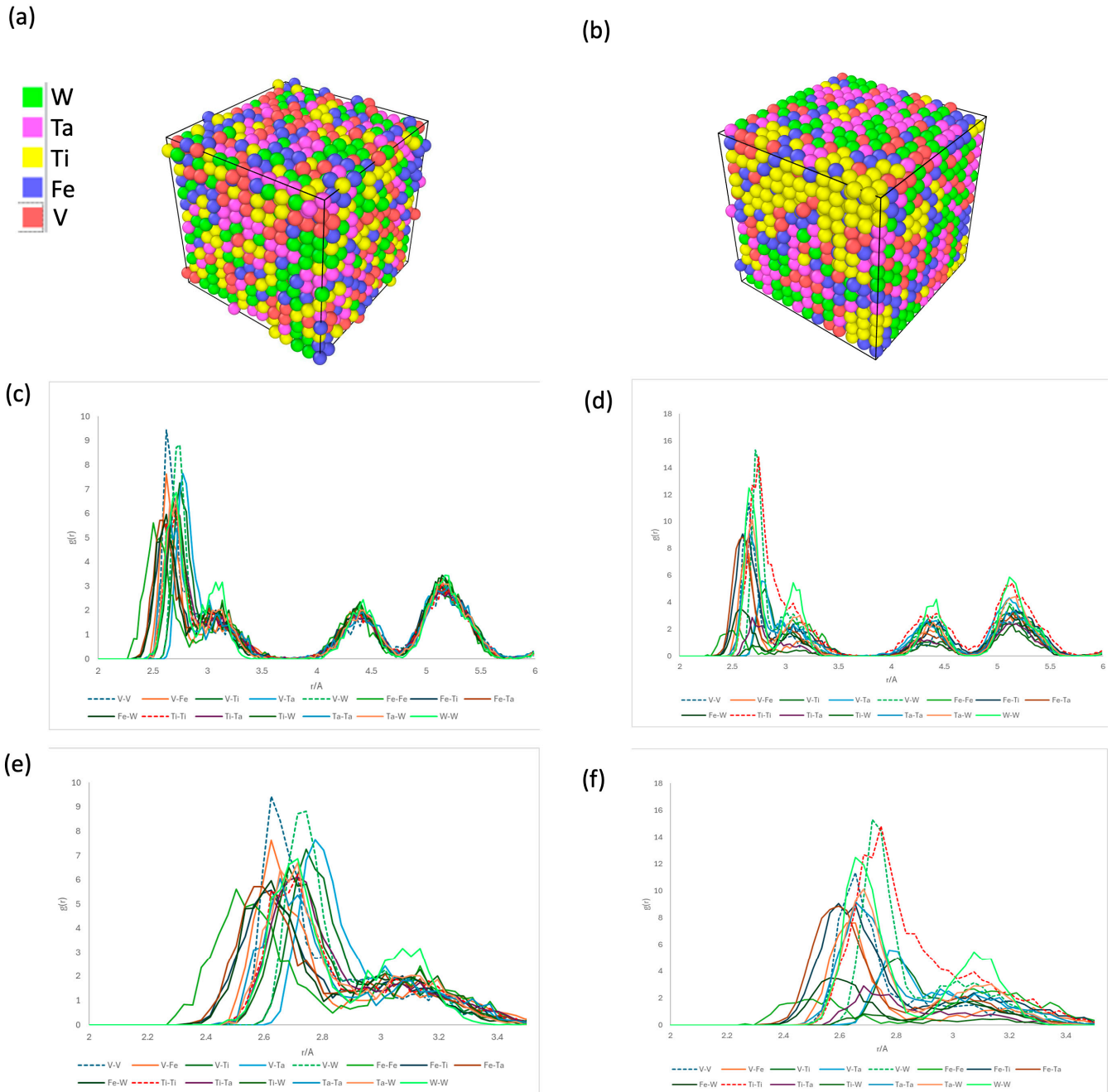


Figure 2. Simulation results at 25 °C (a) MD structure, (b) MC structure, (c,e) MD Pair Distribution Functions, (d,f) MC Pair Distribution Functions.

Figure 3 presents the results of chemical segregation for both types of simulations, MC and MD, as a function of temperature. The same procedure was used in [30], i.e., chemical analysis at 27 locations within the simulation cell to reflect the dispersion of chemical compositions. The MD simulation yields a slight standard deviation, approximately constant with temperature, reflecting the random distribution of the elements. In contrast,

the MC simulation showed a much higher degree of segregation, increasing at intermediate temperature, consistent with element segregation.

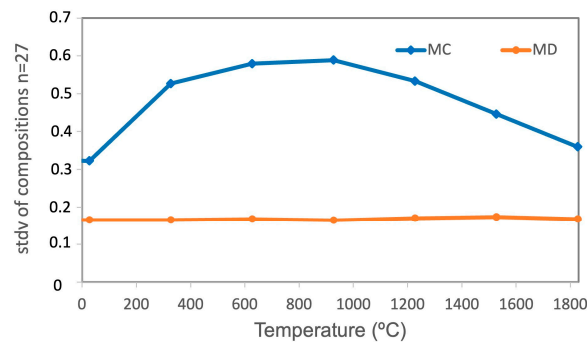


Figure 3. Chemical segregation as function of temperature for MD and MC simulations.

3.2. Powder Analysis of FeTaTiVW

Figure 4 shows the X-ray diffraction together with the SEM images of the milled powder of the FeTaTiVW high entropy alloy. After 2 h of milling, the individual peaks of the elements disappeared, and a bcc-type structure was formed with a lattice parameter of 0.316 nm, very close to pure W, which points to a W not all mixed in the alloy. The formation of a bcc agrees with the thermodynamic calculations and also with MC and MD simulations. The presence of the WC due to the container and the vials was also observed. Furthermore, the presence of TiO₂ was also observed. SEM observations were carried out to confirm the presence of pure W not mixed, as shown in Figure 4c,d. The images revealed that FeTaTiVW milled powder comprised small, agglomerated particles, and no W particles were observed. The phase constitution obtained experimentally as-milled, i.e., a single bcc phase with Ti segregated, albeit in the form of oxide, as seen in XRD, agrees with that predicted by the MC simulation. In addition, the loss of titanium towards oxides observed in XRD may explain the slight deviation of the lattice parameter of the MC simulation, 0.3091 nm, from that obtained experimentally, 0.316 nm.

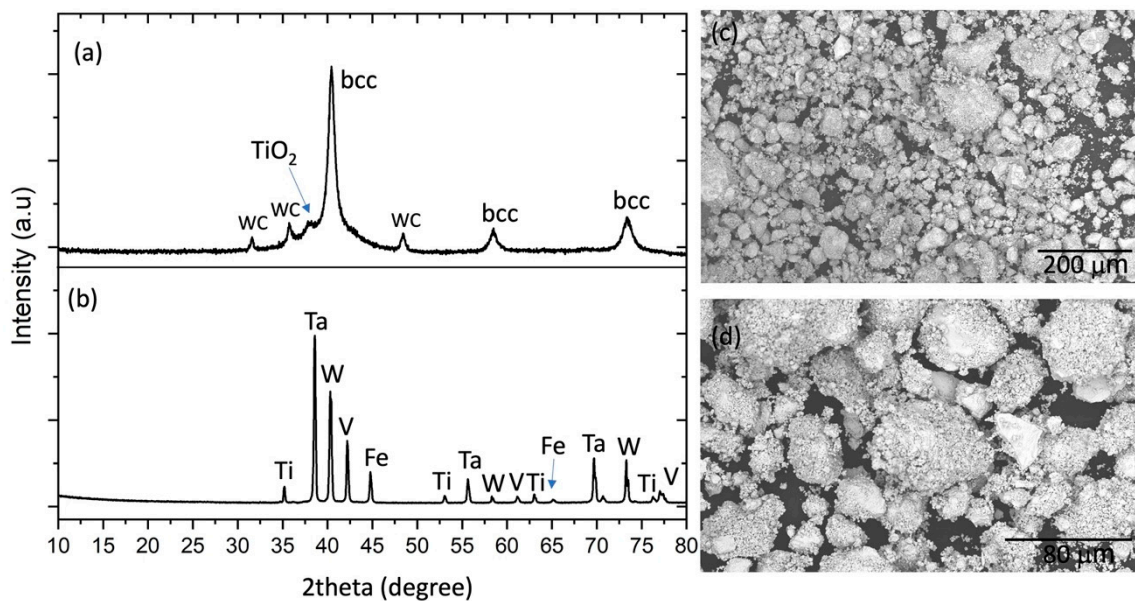


Figure 4. (a,b) X-ray diffraction of FeTaTiVW milled powder and the mixture of pure elements, respectively, and (c,d) SEM images of the FeTaTiVW milled powder of high entropy alloy.

3.3. Consolidated and Annealed FeTaTiVW Material

The microstructure of the consolidated FeTaTiVW high entropy alloy is shown in Figure 5a. The material exhibited a fine microstructure with mixed phases that seem to be a eutectic mixture. In addition, no porosity was observed, which agrees with the 99% calculated apparent density. To understand which phases are present in the microstructure, a heat treatment at 1000 °C for 21 days was performed, as shown in Figure 5b. In fact, comparing the non-treated microstructure with the heat-treated one, it is possible to conclude that annealing induces the globalisation of the phases, and three phases can be distinguished. EDS maps for each element (Figure 5c–g) evidenced the presence of a W-rich phase (indicated by red arrow), a Ti-rich phase (indicated by yellow arrow) and a phase with all elements but with low Ti and W content (indicated by the blue arrow). The observation of W-rich particles on the microstructure may be ascribed to the high melting point of this element, preventing diffusion of this element within the alloy. In fact, the solid solution formed (indicated by the blue arrow) seems to have an atomic percentage of less than 20 for W. Moreover, the enthalpy of mixing elements between constituent atomic pairs ΔH_{mix} AB plays a vital role in phase formation: the more negative ΔH_{mix} , the more significant driving force for forming intermetallic compounds, while the more positive, the more substantial tendency for elemental separation in the alloy. The values of the mixing enthalpy of the atomic pairs are evidenced in Table 4 [32].

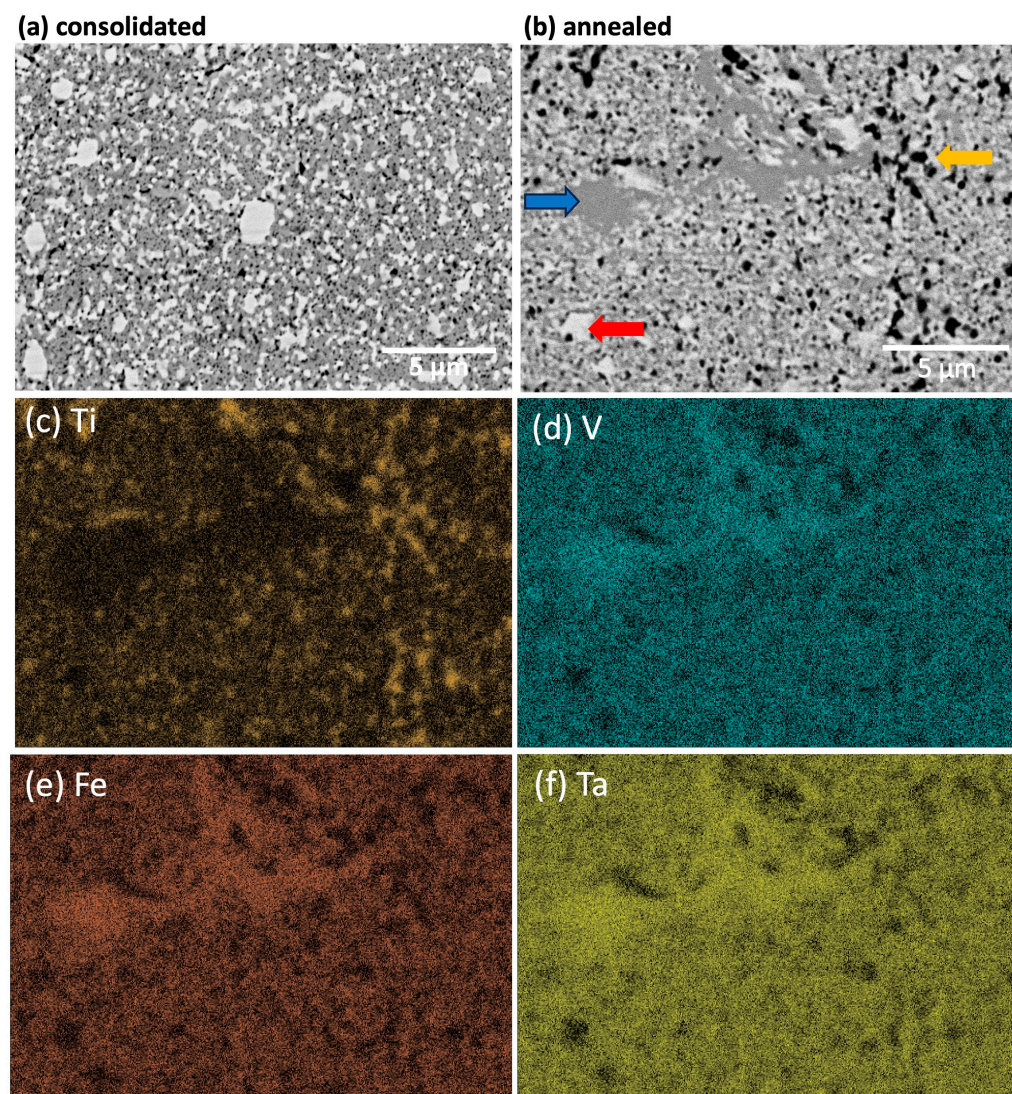


Figure 5. Cont.

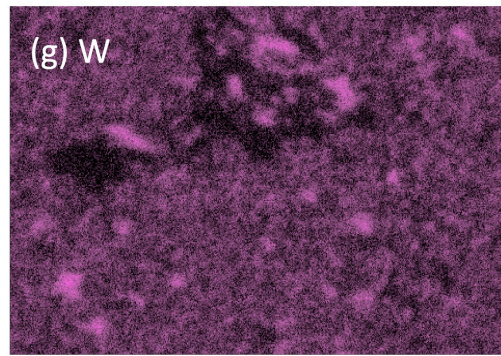


Figure 5. SEM images of the (a) consolidated and (b) annealed FeTaTiVW high entropy alloy and the correspondent EDS maps of the image of (b) for (c) Ti, (d) V, (e) Fe, (f) Ta and (g) W. The arrows shown in (b) evidence three phases with different contrasts.

Table 4. ΔH_{mix} for all the atomic pairs of the FeTaTiVW high entropy alloy.

Atomic Pairs	ΔH_{mix} (kJ/mol)
Fe-Ta	−15
Fe-Ti	−17
Fe-W	0
Ta-Ti	1
Ta-W	−7
Ti-W	−6
V-Fe	−7
V-Ta	−1
V-Ti	−2
V-W	−1

Among all the binary atomic pairs presented in Table 4, the enthalpy of mixing between Ti and the other elements as V and Fe is more negative compared to the other binaries, which implies the formation of a Ti-rich phase as probably an intermetallic one. However, in the case of Fe-Ta, the enthalpy is also large and seems to be associated with the Fe-Ta-V phase with low Ti and W content. Therefore, the consolidated microstructure clearly shows the titanium segregation (Ti-rich phase) within the alloy and confirms the segregation prediction of MC simulation. Moreover, the W-rich phase associated with the low diffusion of W was not considered in the MC simulation since this tool uses element swaps that are not governed by diffusion kinetics but rather by the overall potential energy of the final structure and could not be predicted. Therefore, high melting point elements, with high activation energy for diffusion, may yield different results from those predicted by MC simulation. In contrast, the processing by mechanical alloying evolving essentially deformation mechanisms may be more suited to simulation by the MC process, as was observed for the as-milled powder.

3.4. Differential Thermal Analysis (DTA)

Figure 6 shows the differential thermal analysis of the consolidated FeTaTiVW high entropy alloy. The graph shows that no transformation occurred on the material up to 1300 °C, which allows us to say that the microstructure shown in the above section does not correspond to a eutectic mixture. Since no abrupt transformation was observed, no liquid was formed, and it can be concluded that the fine microstructure presented on the consolidated material in Figure 3 corresponds to transformations in the solid state.

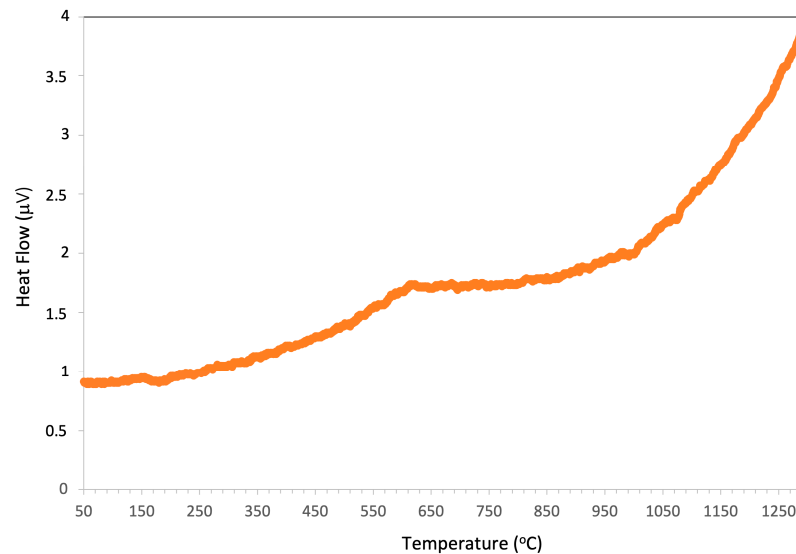


Figure 6. DTA of the consolidated FeTiTaVW sample.

3.5. Thermal Properties

The thermal barrier between the W plasma-facing component and the CuCrZr heat sink should have low thermal conductivity (10–15 W/m/K) to ensure a heat flux of approximately 10 MW/m² [3,33]. Figure 7a shows the thermal conductivity of the FeTiTaVW sample together with the pure W, Cu, and CuCrZr. The results reveal that the FeTiTaVW sample exhibits significantly lower thermal conductivity between 25 °C and 1000 °C than W and CuCrZr, with a value between 15 and 31 (W/(m·K)). In fact, this effect arises from notable alterations in the free paths for electron migration in high entropy alloys and the formation of barriers to electron flow at grain boundaries during heat transfer [34]. In the case of pure W [35] and CuCrZr [35], the high levels of purity lead to unobstructed pathways for electron migration, pointing to higher values of thermal conductivity. Moreover, the values found for the FeTiTaVW high entropy alloy are similar to those found for the case of Al_xCoCrFeNi (0 ≤ x ≤ 2) [36]. Taking into account the targeted thermal conductivities for the thermal barriers (15 W/m/K) [3], it can be inferred that the FeTiTaVW high entropy alloy may be suitable for this purpose, although it is at a higher limit. Figure 7b depicts the specific heat of the FeTaTiVW sample alongside CuCrZr [37] and pure W [38]. Based on the results, the specific heat of FeTaTiVW high entropy alloys around 0.3 (J/g/K), falling between those of CuCrZr and tungsten, remaining relatively constant with increasing temperature. The low specific heat exhibited by CuCrZr and (W) implies less energy required for heating or cooling; positioning FeTaTiVW between them will be crucial for its role as a thermal barrier. Furthermore, results on samples with transition and lanthanide elements revealed [39,40] values of specific heat in the same range found for FeTaTiVW. In addition, Figure 7c exhibits the thermal expansion results of FeTaTiVW sample in the range temperature of 0 to 1000 °C. The thermal expansion increases with temperature and can be attributed to unit cell expansion and the distance increase between lattice sites with increasing temperature. Therefore, the lattice vibration is intensified with an increase in temperature, and consequently, the average distance between atoms within the lattice increases, leading to increased coefficients of thermal expansion [41]. However, compared to the values in the same range for W [32] and CuCrZr [41], the values of CuCrZr above 100 °C are higher than those found for FeTaTiVW high entropy alloy.

In comparison, the values of W are lower than those found for the FeTaTiVW material, making this system's thermal expansion in between W and CuCrZr. In fact, materials with high melting points typically possess strong bonds between their atoms, resulting in lower thermal expansion tendencies. Recent research into the NbTiVZr system [41] reveals thermal expansion rates notably surpassing those of the FeTaTiVW system, falling within the range of [50–200] $\Delta L/L_0 \times 10^{-4}$. This finding unveils intriguing prospects for the

thermal optimisation of FeTaTiVW high entropy alloy through targeted modifications of certain elements or control over elemental concentrations to achieve the desired thermal expansion characteristics.

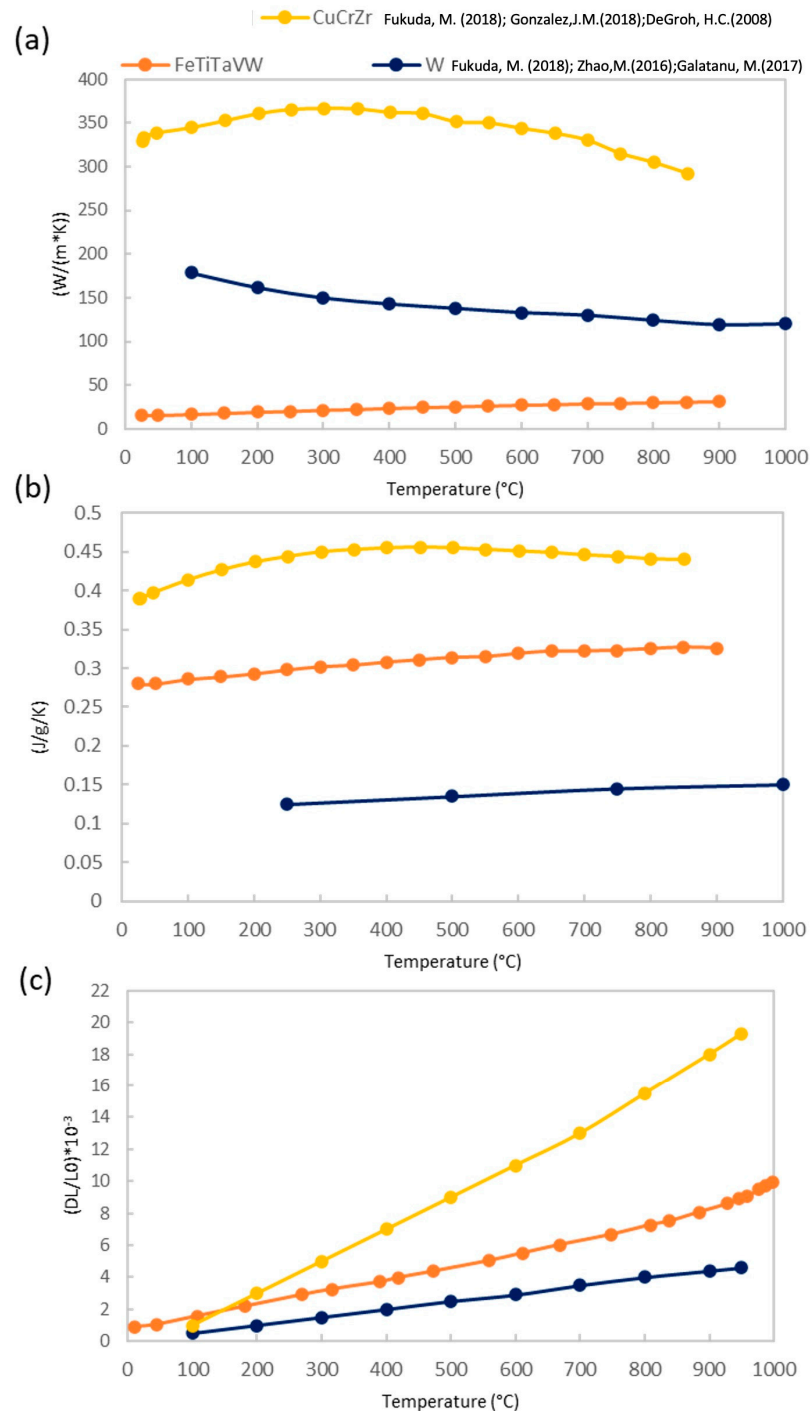


Figure 7. (a) Thermal conductivity of FeTiTaVW consolidated sample together with pure W, adapted from [35] and CuCrZr, adapted from [35], (b) specific heat of FeTiTaVW consolidated sample together with W, adapted from [38] and CuCrZr, adapted from [37], (c) thermal expansion of FeTiTaVW consolidated sample together with W, adapted from [33] and CuCrZr, adapted from [42].

3.6. Mechanical Properties

Figure 8 shows the results of the three-point bending tests for the FeTiTaVW consolidated high entropy alloy, showing the (a) Stress-strain curves at each temperature (25 °C,

600 °C and 1000 °C) and (b) the ultimate flexural strength in all the temperature range. The alloys tested at 25 °C and 600 °C have a linear elastic behaviour and present a brittle fracture. At higher temperatures, 1000 °C, the material shows a different curve, indicating ductile behaviour as presented by [11,43] on W-based refractory HEAs. But, consequently, lower strength values than at lower temperatures. The high ductile-to-brittle-transition temperature (above 600 °C) seems less favourable for structural purposes than that of other refractory high entropy alloys reported in the literature [11].

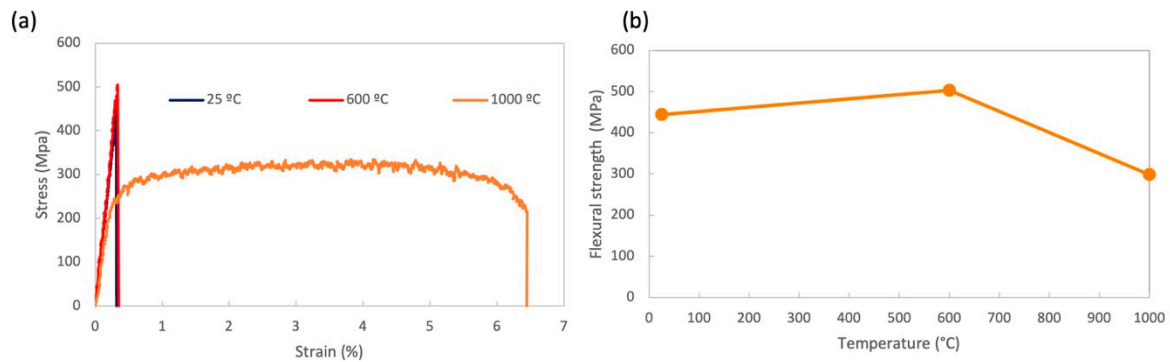


Figure 8. (a) Stress-strain curves for consolidated FeTiTaVW high entropy at 2 °C, 600 °C and 1000 °C and (b) flexural strength fracture as a function of temperature.

Figure 9 shows the surface of the samples after three-point bending tests at 25 °C, 600 °C and 1000 °C, respectively. Brittle facets, i.e., cleavages and river-like structures, can be appreciated at 25 °C and 600 °C, but no agglomerates or visible defects could be identified as crack initiators. However, the micrographs obtained by the three-point bending test at 1000 °C evidence a ductile fracture characterised by micro-void coalescence of varying sizes of about a few microns, as observed in Figure 9c, where macroscopic deformation of the sample section is evident; at higher magnification, no cleavage facets (i.e., river marks, “tongues” or crack-initiation sites) can be appreciated and instead distinct deformed nanograins are observed. These features for ductile fractures are indicative of substantial plastic deformation, as observed in Figure 8, where more than 6% of strain was recorded in all cases.

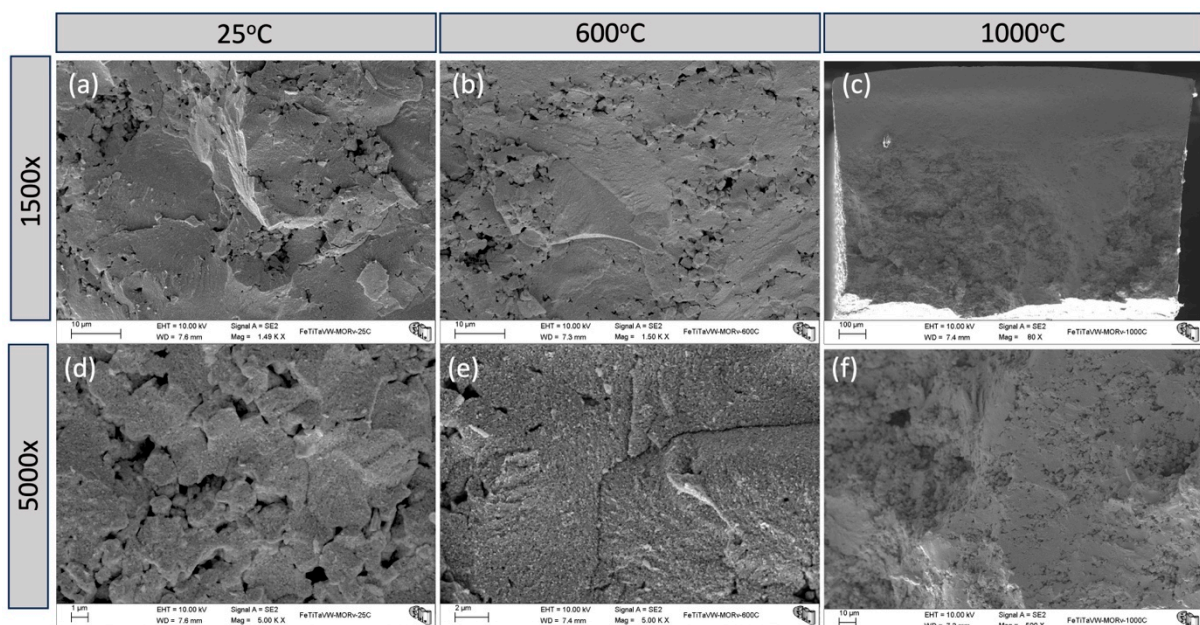


Figure 9. Types of fracture and cleavage facets observed throughout the three test temperatures for FeTiTaVW high entropy at different magnifications for (a,d) 25 °C, (b,e) 600 °C and (c,f) 1000 °C.

The indentation hardness of the sample was measured at 14 ± 2 GPa, while the value of the microscopic indentation was found to be $HV1100 \pm 55$ (10.8 ± 0.5 GPa). The exhibited hardness results for this sample are considerably higher than those reported for other HEAs with similar compositions (mostly in general in the 140 HV to 900 HV), which point to strong atomic bonding and hard crystal structures, such as the intermetallics observed in the XRD microstructural analysis. In fact, HEAs are strengthened by significant lattice distortion, which causes a solid-solution hardening [44]. However, the elastic modulus of the alloy obtained via nanoindentation (210 ± 15 MPa) is lower than that of pure tungsten (400 GPa). All other elements used in this system and CuCrZr are between 116 and 200 GPa. For high entropy alloys, similar values have been displayed, ranging from 100 GPa to 600 GPa [45–47].

4. Conclusions

This work presents structural, thermal characterisation, and simulations for phase prediction of FeTiTaVW high entropy alloys. The MC simulations were more accurate by predicting significant segregation, particularly with a lower potential energy per atom. This segregation suggested by the MC simulation was corroborated by microstructural analysis of the annealed sample, highlighting the presence of a Ti-rich phase. The thermal conductivity of the FeTiTaVW HEA showed a slight increase with temperature while staying lower than CuCrZr and W, remaining within the range of 15 to 31 (W/m/K). Meanwhile, the specific heat measured values that ranged between 0.25 and 0.3 (J/g/K) are between CuCrZr and W. Finally, the thermal expansion values measured between 100–1000 °C increased with temperature and the values are placed between W (the lowest) and CuCrZr (the highest) thermal expansion, which is required for a thermal barrier. The mechanical analysis of the alloy indicates a ductile behaviour at 1000 °C, while at 25 °C and 600 °C it evidences a brittle one. These findings show that the FeTiTaVW HEA is a promising material for applications in nuclear fusion reactors. However, further optimisation of its composition is still required to improve the mechanical properties, and irradiation damage should be evaluated in the near future.

Author Contributions: Conceptualization, M.D. and R.M.; methodology, M.D.; software J.B.C.; Validation, M.D., J.B.C. and E.A.; formal analysis, M.D.; investigation, M.D., A.G., J.B.C., E.T. and J.Y.P.; resources, A.P.G., A.G., E.T. and J.Y.P.; data curation, A.P.G. and A.G.; writing—original draft preparation, R.M., E.T. and M.D.; writing—review and editing, R.M., E.T., M.D. and J.B.C.; visualization, R.M.; supervision, M.D.; project administration, M.D. and E.A.; funding acquisition, M.D., E.A. and J.Y.P. All authors have read and agreed to the published version of the manuscript.

Funding: This research was funded by Fundação para a Ciência e Tecnologia, I.P. by project reference UIDB/50010/2020 (10.54499/UIDB/50010/2020), UIDP/50010/2020 (10.54499/UIDP/50010/2020), project LA/P/0061/2020 (10.54499/LA/P/0061/2020) and “Agencia Estatal de Investigación” under the call “Proyectos de Generación de Conocimiento 2022” (3DPOSTHERMEC, PID2022-137274NB-C33PID). This work has been carried out within the framework of the EUROfusion Consortium, funded by the European Union via the Euratom Research and Training Programme (Grant Agreement No 101052200—EUROfusion). Views and opinions expressed are however those of the author(s) only and do not necessarily reflect those of the European Union or the European Commission. Neither the European Union nor the European Commission can be held responsible for them.

Data Availability Statement: The raw data supporting the conclusions of this article will be made available by the authors on request.

Acknowledgments: IPFN activities were supported by FCT—Fundação para a Ciência e Tecnologia, I.P. by project reference UIDB/50010/2020 and DOI identifier 10.54499/UIDB/50010/2020 (<https://doi.org/10.54499/UIDB/50010/2020>, accessed on 3 March 2024), by project reference UIDP/50010/2020 and DOI identifier DOI 10.54499/UIDP/50010/2020 (<https://doi.org/10.54499/UIDP/50010/2020>, accessed on 3 March 2024) and by project reference LA/P/0061/202 and DOI 10.54499/LA/P/0061/2020 (<https://doi.org/10.54499/LA/P/0061/2020>, accessed on 3 March 2024). Additional support from the Spanish “Agencia Estatal de Investigación” under the call “Proyectos de Generación de Conocimiento 2022” (3DPOSTHERMEC, PID2022-137274NB-C33PID) is also acknowl-

edged. This work has been carried out within the framework of the EUROfusion Consortium, funded by the European Union via the Euratom Research and Training Programme (Grant Agreement No 101052200—EUROfusion). Views and opinions expressed are, however, those of the author(s) only and do not necessarily reflect those of the European Union or the European Commission. Neither the European Union nor the European Commission can be held responsible for them.

Conflicts of Interest: The authors declare no conflict of interest.

References

1. Baluc, N.; Abe, K.; Boutard, J.L.; Chernov, V.M.; Diegele, E.; Jitsukawa, S.; Kimura, A.; Klueh, R.L.; Kohyama, A.; Kurtz, R.J.; et al. Status of R&D activities on materials for fusion power reactors. *Nucl. Fusion* **2007**, *47*, S696–S717. [[CrossRef](#)]
2. Barabash, V.; Peacock, A.; Fabritsiev, S.; Kalinin, G.; Zinkle, S.; Rowcliffe, A.; Rensman, J.W.; Tavassoli, A.A.; Marmy, P.; Karditsas, P.J.; et al. Materials challenges for ITER—Current status and future activities. *J. Nucl. Mater.* **2007**, *367–370 Pt A*, 21–32. [[CrossRef](#)]
3. Barrett, T.R.; McIntosh, S.C.; Fursdon, M.; Hancock, D.; Timmis, W.; Coleman, M.; Rieth, M.; Reiser, J. Enhancing the DEMO divertor target by interlayer engineering. *Fusion Eng. Des.* **2015**, *98–99*, 1216–1220. [[CrossRef](#)]
4. Stork, D.; Agostini, P.; Boutard, J.L.; Buckthorpe, D.; Diegele, E.; Dudarev, S.L.; English, C.; Federici, G.; Gilbert, M.R.; Gonzalez, S.; et al. Developing structural, high-heat flux and plasma facing materials for a near-term DEMO fusion power plant: The EU assessment. *J. Nucl. Mater.* **2014**, *455*, 277–291. [[CrossRef](#)]
5. Sathiaraj, G.D.; Ahmed, M.Z.; Bhattacharjee, P.P. Microstructure and texture of heavily cold-rolled and annealed fcc equiatomic medium to high entropy alloys. *J. Alloys Compd.* **2016**, *664*, 109–119. [[CrossRef](#)]
6. Nong, Z.S.; Lei, Y.N.; Zhu, J.C. Wear and oxidation resistances of AlCrFeNiTi-based high entropy alloys. *Intermetallics* **2018**, *101*, 144–151. [[CrossRef](#)]
7. Gao, M.C.; Zhang, B.; Guo, S.M.; Qiao, J.W.; Hawk, J.A.; Energy, N.; Rouge, B. High-Entropy Alloys in Hexagonal Close Packed Structure. *Metall. Mater. Trans. A* **2016**, *47*, 3322–3332. [[CrossRef](#)]
8. Cantor, B.; Chang, I.T.H.; Knight, P.; Vincent, A.J.B. Microstructural development in equiatomic multicomponent alloys. *Mater. Sci. Eng. A* **2004**, *375–377*, 213–218. [[CrossRef](#)]
9. Yussenko, K.V.; Riva, S.; Carvalho, P.A.; Yussenko, M.V.; Arnaboldi, S.; Sukhikh, A.S.; Hanfland, M.; Gromilov, S.A. First hexagonal close packed high-entropy alloy with outstanding stability under extreme conditions and electrocatalytic activity for methanol oxidation. *Scr. Mater.* **2017**, *138*, 22–27. [[CrossRef](#)]
10. Mukarram, M.; Munir, M.A.; Mujahid, M.; Yaqoob, K. Systematic development of eutectic high entropy alloys by thermodynamic modeling and experimentation: An example of the coCrFeNi-Mo system. *Metals* **2021**, *11*, 1484. [[CrossRef](#)]
11. Senkov, O.N.; Wilks, G.B.; Scott, J.M.; Miracle, D.B. Mechanical properties of Nb₂₅Mo₂₅Ta₂₅W₂₅ and V₂₀Nb₂₀Mo₂₀Ta₂₀W₂₀ refractory high entropy alloys. *Intermetallics* **2011**, *19*, 698–706. [[CrossRef](#)]
12. Zhou, N.; Hu, T.; Huang, J.; Luo, J. Stabilization of nanocrystalline alloys at high temperatures via utilizing high-entropy grain boundary complexions. *Scr. Mater.* **2016**, *124*, 160–163. [[CrossRef](#)]
13. Ayyagari, A.; Salloom, R.; Muskeri, S.; Mukherjee, S. Low activation high entropy alloys for next generation nuclear applications. *Materialia* **2018**, *4*, 99–103. [[CrossRef](#)]
14. Lu, Y.; Huang, H.; Gao, X.; Ren, C.; Gao, J.; Zhang, H.; Zheng, S.; Jin, Q.; Zhao, Y.; Lu, C.; et al. A promising new class of irradiation tolerant materials: Ti₂ZrHfV_{0.5}Mo_{0.2} high-entropy alloy. *J. Mater. Sci. Technol.* **2019**, *35*, 369–373. [[CrossRef](#)]
15. Xie, L.; Brault, P.; Thomann, A.L.; Bauchire, J.M. AlCoCrCuFeNi high entropy alloy cluster growth and annealing on silicon: A classical molecular dynamics simulation study. *Appl. Surf. Sci.* **2013**, *285*, 810–816. [[CrossRef](#)]
16. Widom, M.; Huhn, W.P.; Maiti, S.; Steurer, W. Hybrid molecular dynamic Monte Carlo simulation and experimental production of a multi-component Cu–Fe–Ni–Mo–W alloy/molecular dynamics simulation of a refractory metal high entropy alloy. *Metall. Mater. Trans. A Phys. Metall. Mater. Sci.* **2014**, *45*, 196–200. [[CrossRef](#)]
17. Plimpton, S. Fast parallel algorithms for short-range molecular dynamics. *J. Comput. Phys.* **1995**, *117*, 1–19. [[CrossRef](#)]
18. Coleman, S.P.; Spearot, D.E.; Capolungo, L. Virtual diffraction analysis of Ni [0 1 0] symmetric tilt grain boundaries. *Model. Simul. Mater. Sci. Eng.* **2013**, *21*, 055020. [[CrossRef](#)]
19. Jelinek, B.; Groh, S.; Horstemeyer, M.F.; Houze, J.; Kim, S.G.; Wagner, G.J.; Moitra, A.; Baskes, M.I. Modified embedded atom method potential for Al, Si, Mg, Cu, and Fe alloys. *Phys. Rev. B* **2012**, *85*, 245102. [[CrossRef](#)]
20. Sharma, A.; Singh, P.; Johnson, D.D.; Liaw, P.K.; Balasubramanian, G. Atomistic clustering-ordering and high-strain deformation of an Al_{0.1}CrCoFeNi high-entropy alloy. *Sci. Rep.* **2016**, *6*, 31028. [[CrossRef](#)]
21. NIST. *Interatomic Potentials Repository*; NIST: Gaithersburg, MD, USA, 2010.
22. Zhou, X.W.; Johnson, R.A.; Wadley, H.N.G. Misfit-energy-increasing dislocations in vapor-deposited CoFe/NiFe multilayers. *Phys. Rev. B* **2004**, *69*, 144113. [[CrossRef](#)]
23. Jacobson, D.W.; Thompson, G.B. Revisiting Lennard Jones, Morse, and N-M potentials for metals. *Comput. Mater. Sci.* **2022**, *205*, 111206. [[CrossRef](#)]
24. Fujii, K. Precision density measurements of solid materials by hydrostatic weighing. *Meas. Sci. Technol.* **2006**, *17*, 2551–2559. [[CrossRef](#)]

25. Heydari, H.; Tajally, M.; Habibolahzadeh, A. Computational analysis of novel AlLiMgTiX light high entropy alloys. *Mater. Chem. Phys.* **2022**, *280*, 125834. [[CrossRef](#)]
26. Oliver, W.C.; Pharr, G.M. An improved technique for determining hardness and elastic modulus using load and displacement sensing indentation experiments. *J. Mater. Res.* **1992**, *7*, 1564–1583. [[CrossRef](#)]
27. Oliver, W.C.; Pharr, G.M. Measurement of hardness and elastic modulus by instrumented indentation: Advances in understanding and refinements to methodology. *J. Mater. Res.* **2004**, *19*, 3–20. [[CrossRef](#)]
28. Guo, S.; Liu, C.T. Phase stability in high entropy alloys: Formation of solid-solution phase or amorphous phase. *Prog. Nat. Sci. Mater. Int.* **2011**, *21*, 433–446. [[CrossRef](#)]
29. Zhang, Y.; Zhou, Y.J.; Lin, J.P.; Chen, G.L.; Liaw, P.K. Solid-solution phase formation rules for multi-component alloys. *Adv. Eng. Mater.* **2008**, *10*, 534–538. [[CrossRef](#)]
30. Dias, M.; Carvalho, P.A.; Gonçalves, A.P.; Alves, E.; Correia, J.B. Hybrid molecular dynamic Monte Carlo simulation and experimental production of a multi-component Cu–Fe–Ni–Mo–W alloy. *Intermetallics* **2023**, *161*, 107960. [[CrossRef](#)]
31. Martins, R.; Gonçalves, A.P.; Correia, J.B.; Galatanu, A.; Alves, E.; Dias, M. Simulation and study of the milling parameters on CuFeTaTiW multicomponent alloy. *Nucl. Mater. Energy* **2023**, *38*, 101568. [[CrossRef](#)]
32. Aghababaii, S.; Shobeiri, F.; Hosseinipanah, S.M. Classification of Bulk Metallic Glasses by Atomic Size Difference, Heat of Mixing and Period of Constituent Elements and Its Application to Characterization of the Main Alloying Element Akira. *J. Postgrad. Med. Inst.* **2016**, *30*, 80–83.
33. Galatanu, M.; Enculescu, M.; Ruiu, G.; Popescu, B.; Galatanu, A. Cu-based composites as thermal barrier materials in DEMO divertor components. *Fusion Eng. Des.* **2017**, *124*, 1131–1134. [[CrossRef](#)]
34. Chen, J.K.; Hung, H.Y.; Wang, C.F.; Tang, N.K. Thermal and electrical conductivity in Al–Si/Cu/Fe/Mg binary and ternary Al alloys. *J. Mater. Sci.* **2015**, *50*, 5630–5639. [[CrossRef](#)]
35. Fukuda, M.; Hasegawa, A.; Nogami, S. Thermal properties of pure tungsten and its alloys for fusion applications. *Fusion Eng. Des.* **2018**, *132*, 1–6. [[CrossRef](#)]
36. Chou, H.P.; Chang, Y.S.; Chen, S.K.; Yeh, J.W. Microstructure, thermophysical and electrical properties in $\text{Al}_x\text{CoCrFeNi}$ ($0 \leq x \leq 2$) high-entropy alloys. *Mater. Sci. Eng. B Solid-State Mater. Adv. Technol.* **2009**, *163*, 184–189. [[CrossRef](#)]
37. Gonzalez, J.M.; Chiumenti, M.; Cervera, M.; Agelet de Saracibar, C.; Samaniego, F.; Cobo, I. Numerical analysis of the manufacturing processes of a mock-up of the ITER NHF First Wall Panel. *Fusion Eng. Des.* **2018**, *135*, 65–73. [[CrossRef](#)]
38. Zhao, M.; Zhou, Z.; Zhong, M.; Tan, J.; Lian, Y.; Liu, X. Thermal shock behavior of fine grained $\text{W-Y}_2\text{O}_3$ materials fabricated via two different manufacturing technologies. *J. Nucl. Mater.* **2016**, *470*, 236–243. [[CrossRef](#)]
39. Sun, Z.; Shi, C.; Gao, L.; Lin, S.; Li, W. Thermal physical properties of high entropy alloy $\text{Al}_{0.3}\text{CoCrFeNi}$ at elevated temperatures. *J. Alloys Compd.* **2022**, *901*, 163554. [[CrossRef](#)]
40. Xue, Y.; Zhao, X.; An, Y.; Wang, Y.; Gao, M.; Zhou, H.; Chen, J. High-entropy $(\text{La}_{0.2}\text{Nd}_{0.2}\text{Sm}_{0.2}\text{Eu}_{0.2}\text{Gd}_{0.2})_2\text{Ce}_2\text{O}_7$: A potential thermal barrier material with improved thermo-physical properties. *J. Adv. Ceram.* **2022**, *11*, 615–628. [[CrossRef](#)]
41. Jia, Y.; Zhang, L.; Li, P.; Ma, X.; Xu, L.; Wu, S.; Jia, Y.; Wang, G. Microstructure and Mechanical Properties of Nb–Ti–V–Zr Refractory Medium-Entropy Alloys. *Front. Mater.* **2020**, *7*, 1–11. [[CrossRef](#)]
42. DeGroh, H.C.; Ellis, D.L.; Loewenthal, W.S. Comparison of GRCo-84 to other Cu alloys with high thermal conductivities. *J. Mater. Eng. Perform.* **2008**, *17*, 594–606. [[CrossRef](#)]
43. Xiang, L.; Guo, W.; Liu, B.; Fu, A.; Li, J.; Fang, Q.; Liu, Y. Microstructure and Mechanical Properties of TaNbVTiAl refractory high entropy alloys. *Entropy* **2020**, *1*, 282. [[CrossRef](#)]
44. Song, H.; Tian, F.; Hu, Q.M.; Vitos, L.; Wang, Y.; Shen, J.; Chen, N. Local lattice distortion in high-entropy alloys. *Phys. Rev. Mater.* **2017**, *1*, 023404. [[CrossRef](#)]
45. Cui, K.; Zhang, Y. High-Entropy Alloy Films. *Coatings* **2023**, *13*, 635. [[CrossRef](#)]
46. Dada, M.; Popoola, P.; Mathe, N.; Adeosun, S.; Pityana, S. Investigating the elastic modulus and hardness properties of a high entropy alloy coating using nanoindentation. *Int. J. Light. Mater. Manuf.* **2021**, *4*, 339–345. [[CrossRef](#)]
47. Laplanche, G.; Gadaud, P.; Bärsch, C.; Demtröder, K.; Reinhart, C.; Schreuer, J.; George, E.P. Elastic moduli and thermal expansion coefficients of medium-entropy subsystems of the CrMnFeCoNi high-entropy alloy. *J. Alloys Compd.* **2018**, *746*, 244–255. [[CrossRef](#)]

Disclaimer/Publisher’s Note: The statements, opinions and data contained in all publications are solely those of the individual author(s) and contributor(s) and not of MDPI and/or the editor(s). MDPI and/or the editor(s) disclaim responsibility for any injury to people or property resulting from any ideas, methods, instructions or products referred to in the content.